Russian Journal of Earth Sciences

Effects of Source Directivity Observed in the Near-Fault Zones of Large Earthquakes and Accounting for the Effects in Seismic Hazard Analysis and Building Codes

O. V. Pavlenko* and **V. A. Pavlenko**

Schmidt Institute of Physics of the Earth, Russian Academy of Sciences, Moscow, Russia
* **Correspondence to:** Olga Pavlenko, olga@ifz.ru

Abstract: The effects of radiation directivity of finite-fault sources of strong earthquakes have been recognized for a long time. However, only in recent decades, with the development of dense networks of seismic observation, representative data become available, allowing for a detailed study of these effects. Since the 2000s, seismologists have found evidence of super-shear crack propagation in strong earthquakes, resulting in shock fronts (Mach cones) formed by the interference of seismic waves radiated by the crack tip. This phenomenon leads to high peak ground acceleration (PGA) and peak ground velocity (PGV) values recorded in the near-fault zones. In such cases, significant damage occurs in the near-fault zones due to high-amplitude narrow velocity pulses impacting buildings (on fault-parallel components), followed by shaking of another type, caused by trailing Rayleigh ruptures (with dominant fault-normal components). This double punch effect can be particularly destructive to structures. Such phenomena were observed during the earthquakes in Turkey in February 2023. During large subduction earthquakes, due to the geometry of the fault plane, constructive interference of seismic waves and the formation of shock wave fronts are possible without super-shear crack propagation, i.e., with its propagation at normal velocity. Shock fronts were also observed but at considerable distances from the faults, where the resulting damage was relatively minor. This reduced impact is attributed to the high-frequency nature of the strong motions, which pose less risk to buildings. Additionally, the shock fronts, being farther from the sources, were weakened by attenuation mechanisms. Such phenomena are typically observed on large faults with small amounts of asperities, i.e., on faults where earthquakes occur regularly, and asperities are smoothed out, for example, on the North Anatolian and East Anatolian faults in Turkey, on active faults in Tibet, and during large subduction earthquakes.

Keywords: Directivity effects, pulse-like waveforms, large subduction and crustal earthquakes, seismic hazard analysis, abnormally high PGA and PGV

Citation: Pavlenko O. V. and Pavlenko V. A. (2025), Effects of Source Directivity Observed in the Near-Fault Zones of Large Earthquakes and Accounting for the Effects in Seismic Hazard Analysis and Building Codes, *Russian Journal of Earth Sciences*, 25, ES6025, EDN: GLYIDO, https://doi.org/10.2205/2025es001046

Research Article

Received: October 31, 2024
Accepted: June 30, 2025
Published: December 30, 2025

Introduction

Effects of radiation directivity of finite-fault sources of large earthquakes have been studied since the 1980s. *Archuleta and Hartzell* [1981] noted that "the database of strong motion records from sites near moderately large earthquakes increases, and ... to analyze such records, a clear understanding is needed of the complications that arise when one is no longer in the far-field but situated close to a finite rupture ... when the receiver is near the source, so that the radiation originates over some area, the receiver distance, radiation pattern, and arrival times of *P*- and *S*- waves are ill defined, and ... the ground motion cannot be interpreted using the same approach that was appropriate for the far-field". Numerical simulation of high-frequency ground motions revealed a strong influence of directivity effects on acceleration amplitudes in the near-fault zones during the 1979 Imperial Valley earthquake, where peak ground accelerations (PGA) reached approximately 1195 cm/s^2, exceeding 1g [*Archuleta and Hartzell*, 1981].

Somerville et al. [1997] were among the first who developed methods to account for directivity effects in seismic hazard estimation. They noted that "directivity effects occur when the propagation of rupture toward a site at a velocity that is almost as large as the shear wave velocity causes most of the seismic energy from the rupture to arrive in a single large pulse of motion, which represents the cumulative effect of almost all of the seismic radiation from the fault; this should be taken into account when predicting the ground motion in the near-fault zones" [*Somerville et al.*, 1997].

From the viewpoint of physics, directivity effects during strong earthquakes are due to the finite sizes of the fault planes: the rupture does not appear instantly; it starts at some point, the hypocenter, and spreads at a velocity that is usually less than *S*-wave velocity, so that the rupture propagation on the fault plane has some duration. The duration obviously increases with increasing earthquake magnitude, which is clearly seen, for example, when comparing the acceleration time histories of the 2011 Tohoku earthquake, the 1999 Chi-Chi earthquake, and the 2008 Iwate–Miyagi Nairiku earthquake.

Time interval, during which direct *S*-waves arrive at the station can be shortened or increased, depending on the direction of crack propagation relative to the seismic station. Directivity affects both high-frequency and low-frequency components of strong motions. At low frequencies, directivity produces coherent, potentially very destructive high-amplitude pulses. At high frequencies, directivity causes seismic waves to reach seismic station over short time intervals, in the limiting case – almost simultaneously, in the form of Mach cone, shock wave.

Although directivity effects have been recognized for a long time, it is only in recent decades, with the development of dense seismic observation networks, that we have obtained strong motion records in near-fault zones. This advancement has enabled a detailed study of directivity effects, including their impact on the distribution of PGA in near-fault zones, soil behavior, and the response of engineering structures – knowledge essential for seismic hazard assessment and the development of standards of earthquake-resistant design and construction.

This paper describes observations of directivity effects during large subduction and crustal earthquakes, using examples of earthquakes in Japan and Turkey. The methods for incorporating these effects into seismic hazard assessments and building codes are also discussed.

Effects of Radiation Directivity of the Sources of Large Subduction Earthquakes

Directivity effects were observed during all recent large subduction earthquakes in Japan, as can be seen from the records obtained in the near-fault zones. The features of strong motion caused by directivity effects during large subduction earthquakes include: a mosaic pattern of PGA distribution in near-fault zones, independent of soil conditions, instead of a gradual decrease with distance from the fault; hardening of soft soils during strong motion accompanied by high-frequency vibrations, instead of softening and low-frequency vibrations in areas located in the direction of rupture propagation; and the generation of abnormally high PGA in these forward-propagation areas, regardless of soil conditions.

The Tohoku Subduction Earthquake of March 11, 2011

The Tohoku subduction earthquake of March 11, 2011 with moment magnitude $M_w = 9.1$ was the strongest seismic event ever recorded in Japan (Figure 1). 19 K-NET and KiK-net strong motion stations recorded abnormally high PGA values exceeding 1g and reaching ~3g – "anomalously strong motions that we have never seen before" [*Furumura et al.*, 2011]. As shown in Figure 1, the highest PGA values occurred not only near the source, but mostly at rather large distances from the fault, to the south-west of the epicenter.

Based on the records of KiK-net vertical arrays, models of soil behavior were constructed, i.e., vertical distributions of stresses and strains in soil layers [*Pavlenko*, 2016]. The method originally developed by [*Pavlenko and Irikura*, 2003], and previously applied

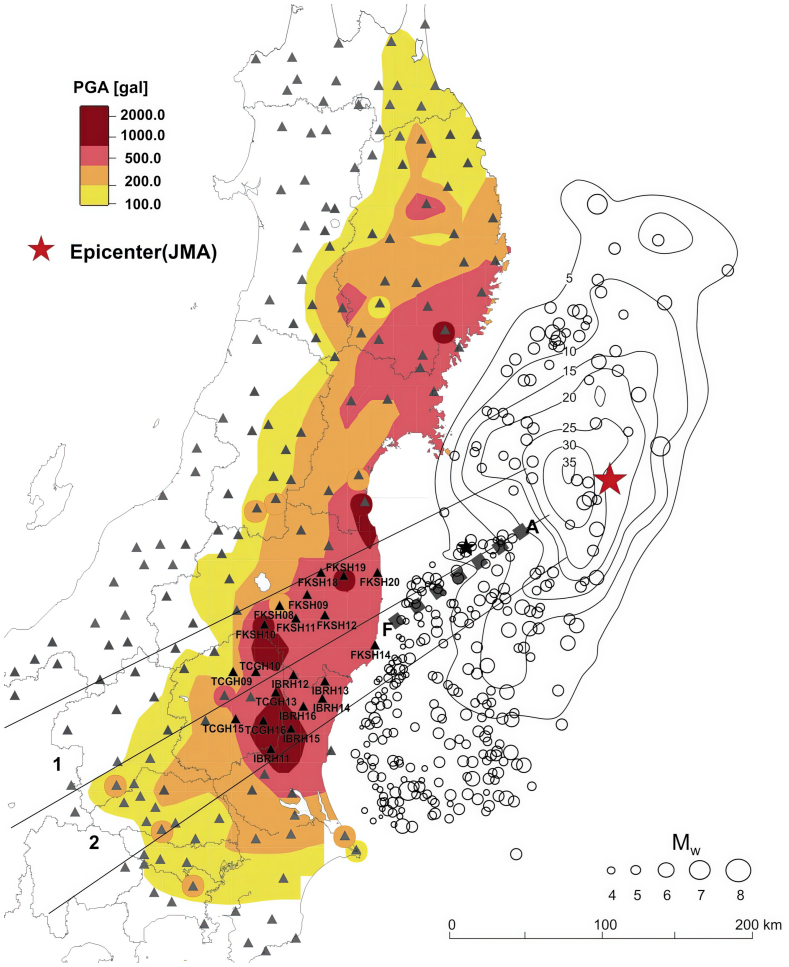

Figure 1. Map showing the distribution of PGA recorded during the Tohoku earthquake [*NIED*, 2011], locations of the mainshock (star) and aftershocks (circles) ($M_w > 3$), recorded during the first 24 hours after the mainshock, and KiK-net stations on Honshu Island: black triangles – studied in this research, gray triangles – other stations. Contour lines show slip distribution over the fault plane according to the model by [*Koketsu et al.*, 2011]. Dotted line indicates the direction of crack propagation to the south-west. Straight lines delimit sectors 1 and 2, where directivity effects are clearly seen in the recorded acceleration time histories [*Pavlenko*, 2017].

to study soil behavior during past strong earthquakes such as the 1995 Kobe earthquake ($M_w = 6.8$) and the 2000 Tottori earthquake ($M_w = 6.7$) [*Pavlenko and Irikura*, 2003, 2006], was used in this analysis. Records of deep devices of the vertical arrays were used as input motions, and motions on the surface were calculated. During these calculations, stress-strain relations in soil layers were selected to achieve the best agreement between calculated and observed surface motions (Figure 2).

There was no strong or widespread nonlinearity in the behavior of soft soils. Typical manifestations of nonlinearity and reduction of shear moduli during strong motion were observed at coastal sites located near the fault. At remote sites, where maximum PGA values were recorded, on soft and dense soils, shear moduli in soil layers increased with the beginning of strong motion, reaching their maxima at the moments of the highest intensity of strong motion, indicating soil hardening. Subsequently, the shear moduli decreased as the intensity of strong motion diminished (Figure 2). At soft soil sites, reduction of shear moduli was accompanied by a stepwise decrease in the predominant frequencies of motion on the surface (Figure 3).

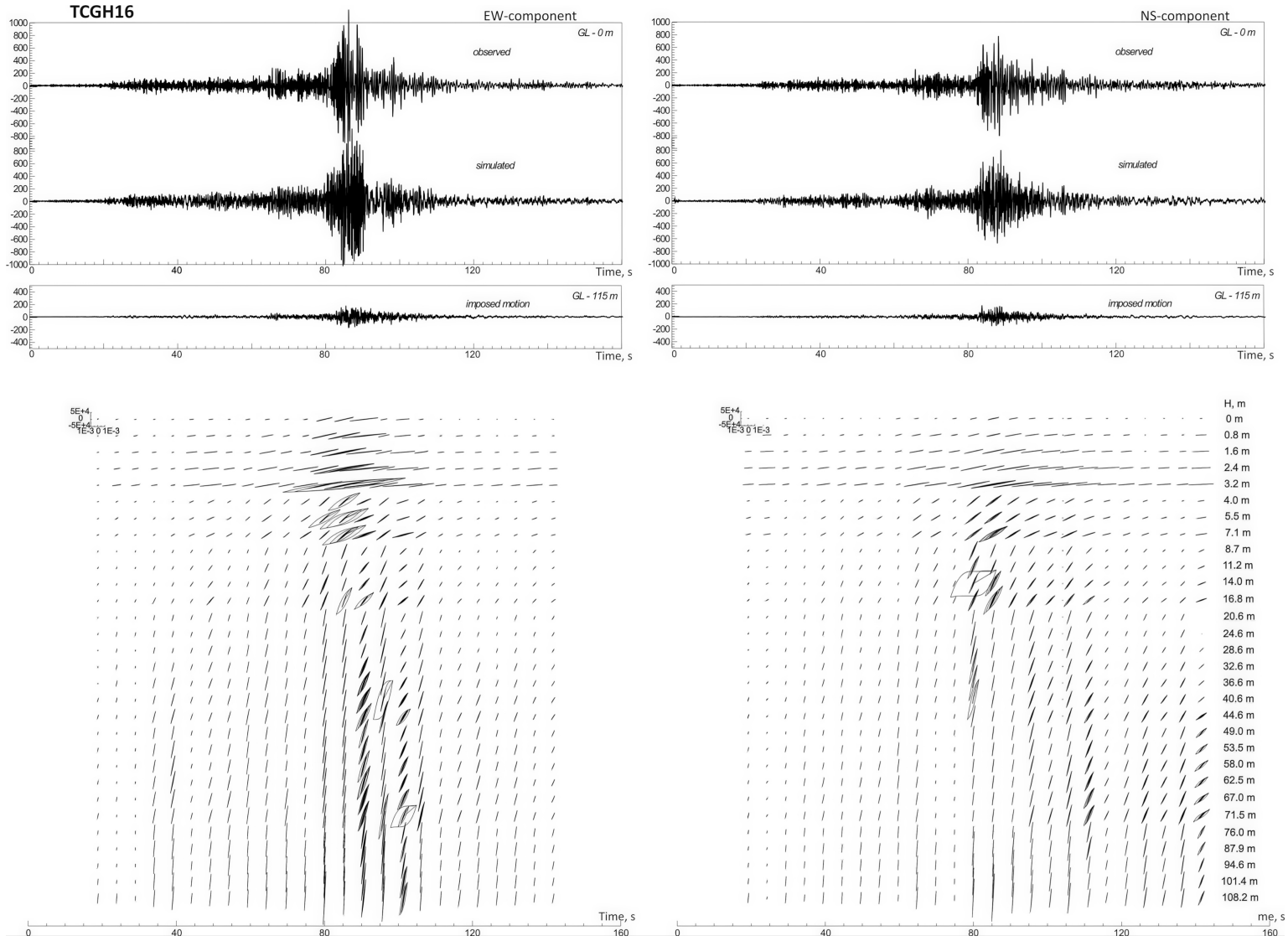

Figure 2. Models of soil behavior at TCGH16 site. Upper row: recorded and simulated acceleration time histories on the surface. Lower row: stress-strain relations in soil layers, changing with time during ~120 s of strong motion, from the surface down to the location of the deep device of the vertical array [from *Pavlenko*, 2016] (108.2 m). Each curve corresponds to 5-second time interval. 0 corresponds to the beginning of the analyzed interval of strong motion.

Strong motions mostly remained high-frequency ones, even on soft soils; as a result "the amount of shaking damage was not great" [*Furumura et al.*, 2011]. This outcome was explained by the relatively low amplitudes of strong motions within the critical frequency range of 0.5 to 1 Hz.

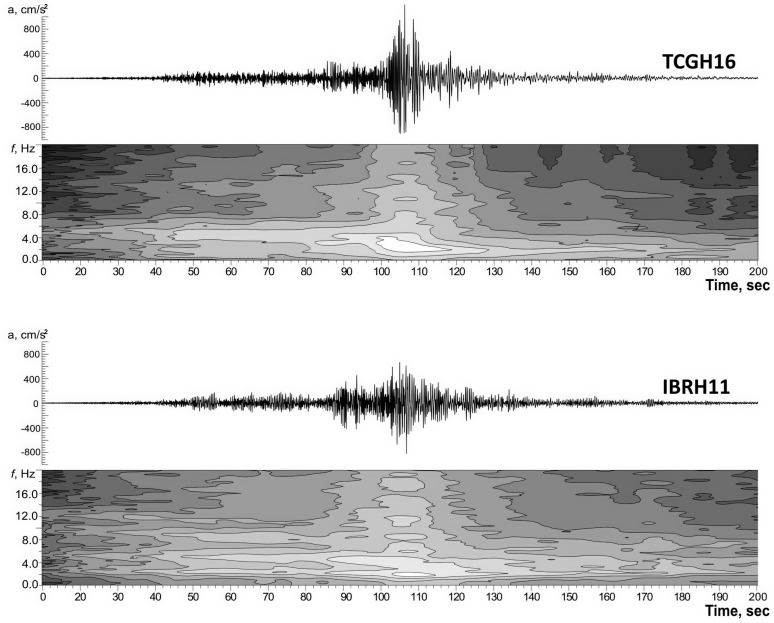

Figure 3. A stepwise drop of the predominant frequencies of motion at soft soil sites that recorded high PGA > 1g during the Tohoku earthquake.

Various authors have proposed models of the temporal evolution of the earthquake source. However, after approximately one minute, most results indicate a unilateral crack propagation to the south-west [*Tajima et al.*, 2013]. *Ide et al.* [2011] estimated the durations of phases of the source process: an initial deep slip lasting ~40 s was followed by an extensive shallow slip over the next 60 to 70 s, and then a prolonged deep slip lasting more than 100 s. Isochrones from the models by different authors reveal the propagation of a large rupture in a south-west direction, similar to that shown by the dotted line in Figure 1. Additionally, post-seismic events triggered by the Tohoku earthquake systematically spread in the same south-west direction [*Miyazawa*, 2011].

In cases of super-shear crack propagation, shock waves are formed because the distance between the crack tip and the seismic stations decreases faster than *S*-waves propagate. Consequently, seismic waves radiated by the crack tip over extended periods of time reach the seismic stations almost simultaneously [etc., *Bouchon et al.*, 2001; *Dunham and Bhat*, 2008; *Zeng et al.*, 2022]. This leads to interference and overlapping of seismic waves, resulting in shock waves, which represent a limiting case of directivity effects.

During the Tohoku earthquake, the mechanism was similar [*Pavlenko*, 2017]. This can be traced by the changes in the waveforms of acceleration time histories recorded at stations located within narrow sectors 1 and 2 (Figure 1), as the distance from the fault increases. The intensity of motion and PGA do not noticeably change within ~300 km from the epicenter, while the duration of strong motion decreases (Figure 4). The duration of strong motion is minimal, and the intensity is maximal at the TCGH16 and IBRH11 sites, at epicentral distances of ~290 to 310 km, indicating a limiting case of directivity effects, a shock wave. It disappears at larger distances, of ~300 to 310 km, where PGA values sharply decrease (Figures 1 and 4).

The cross-section of the fault plane of the Tohoku earthquake and locations of some KiK-net stations are shown in Figure 5. Simple calculations confirm that superposition of seismic waves could occur at KiK-net sites, distant from the fault, due to the size and orientation of the fault plane, and in this case, the crack tip velocity could have sub-Rayleigh values of ~4 km/s.

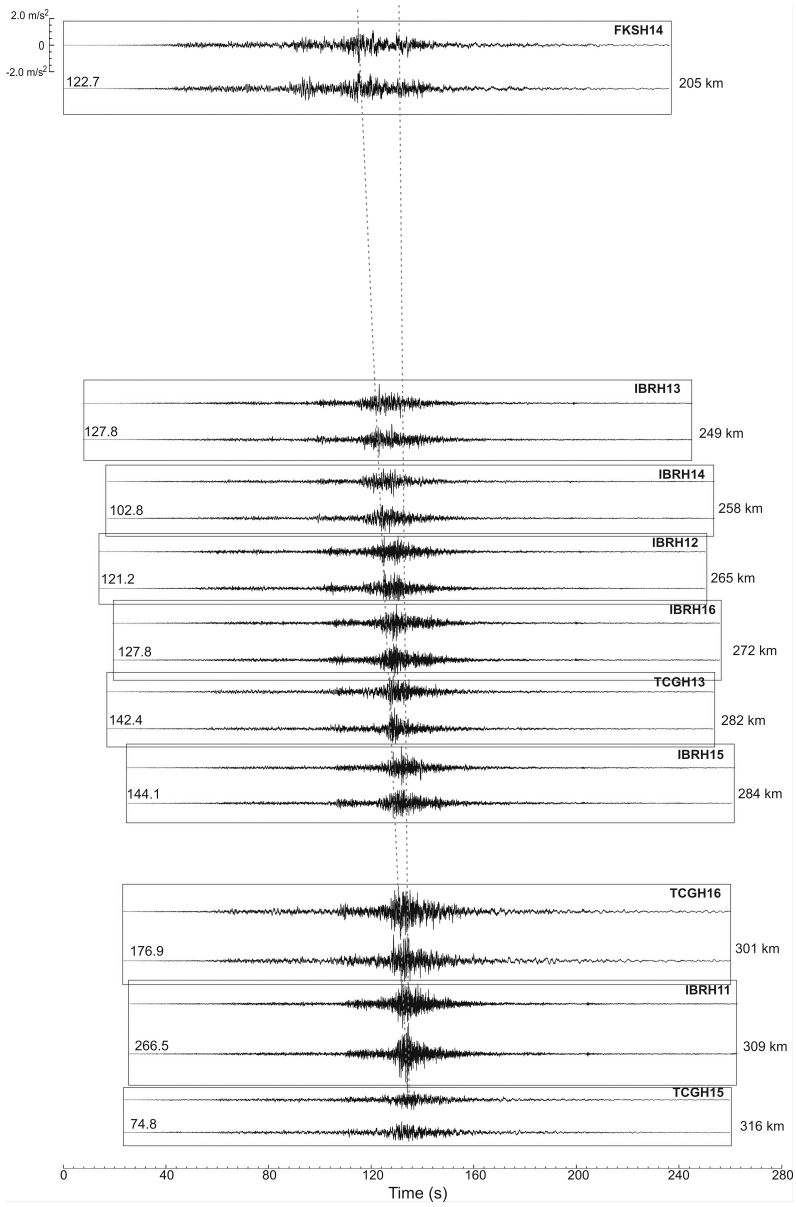

Figure 4. Acceleration time histories of the Tohoku earthquake at horizontal components (records of deep devices of the vertical arrays in sector 2, indicated in Figure 1), arranged according to the distance from the source (vertically) and to the beginning of strong motion (horizontally). Numbers on the left show PGA values in cm/s^2 [from *Pavlenko*, 2017]. Dotted lines show the decrease of strong motion duration with distance.

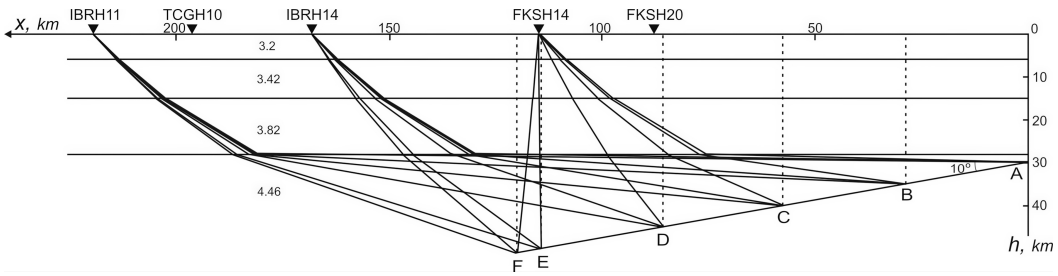

Figure 5. The scheme showing the propagation of seismic waves radiated by the crack tip to seismic stations FKSH14, IBRH14, and IBRH11 [from *Pavlenko*, 2017].

The Tokachi-Oki Subduction Earthquake of September 26, 2003

Similar effects were observed during the 2003 Tokachi-oki subduction earthquake (M_w = 8.3) [*Pavlenko*, 2022]. Figures 6 through 9 present the mosaic distribution of PGA in the near-fault zones of the earthquake, models of soil behavior at remote stations that recorded high PGA, indicating hardening of soft soils, acceleration time histories demonstrating directivity effects, and schemes of the propagation of seismic waves radiated by the crack tip to stations KSRH09, KSRH06, and KSRH10.

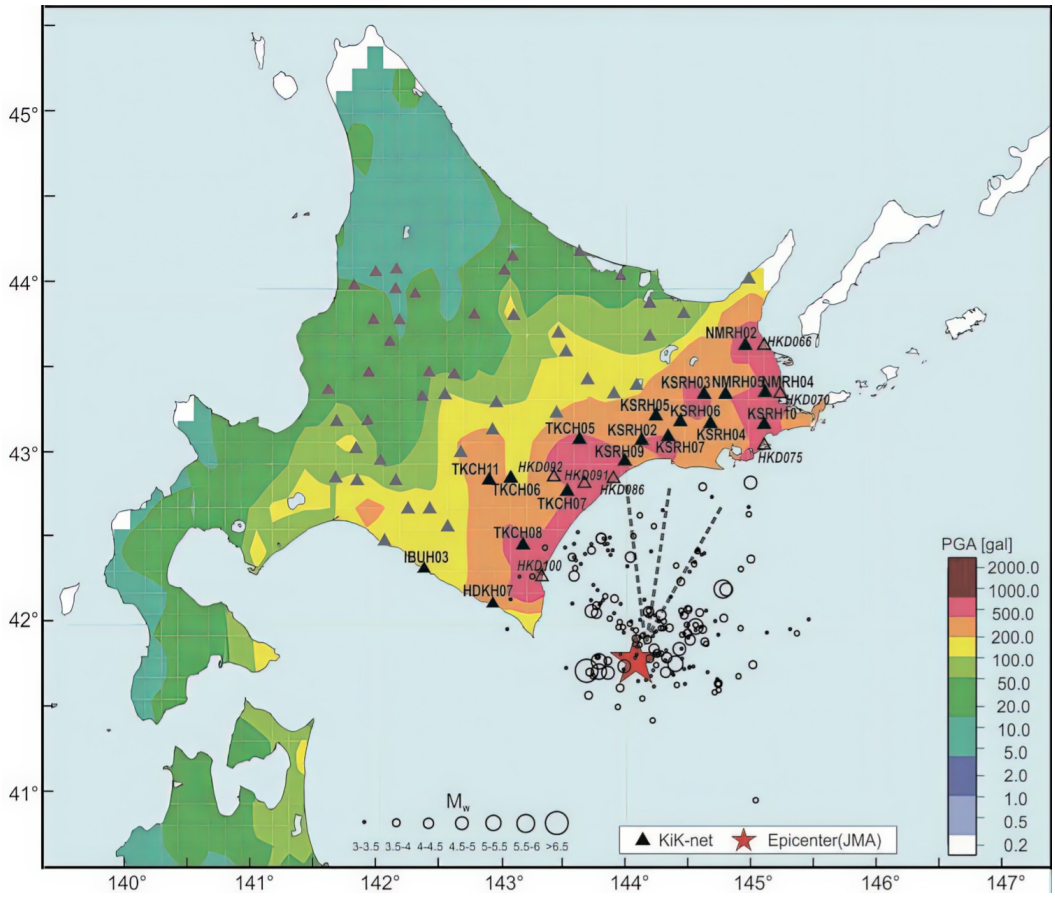

Figure 6. Map showing the distribution of PGA recorded during the 2003 Tokachi-oki earthquake (NIED data), locations of the mainshock (star), aftershocks (circles) (M_w > 3) that occurred in 24 hours after the mainshock (JMA data), and KiK-net stations (triangles). Dotted lines show horizontal projections of the rupture propagation towards KSRH09, KSRH06, and KSRH10 sites [from *Pavlenko*, 2022].

Similar to the Tohoku earthquake, strong motion records of the 2003 Tokachi-oki earthquake do not show widespread nonlinearity of soft soil behavior. Manifestations of soil nonlinearity and reduction of shear moduli during strong motion were observed at stations located near the source. At remote stations that recorded high PGA (KSRH03, KSRH10, NMRH02, NMRH04), soil behavior was virtually linear; shear moduli in soil layers reached their maxima during the moments of the highest intensity of motion, showing soil hardening, then reduced with decreasing intensity of strong motion (Figure 7).

The waveforms of the acceleration time histories indicate the effects of radiation directivity (Figure 8), i.e., overlapping of seismic waves at remote stations, when the waves radiated by the crack tip during its propagation along a section of the fault plane arrived at remote stations almost simultaneously. These motions caused hardening of soft soils and therefore, increase of amplification of seismic waves in soil layers, resulting in high PGA on the surface. Calculations testify that superposition of seismic waves could occur at stations distant from the source due to the size and orientation of the fault plane, and the velocity of crack propagation could have sub-Rayleigh values of ~4.0 to 4.3 km/s in this case.

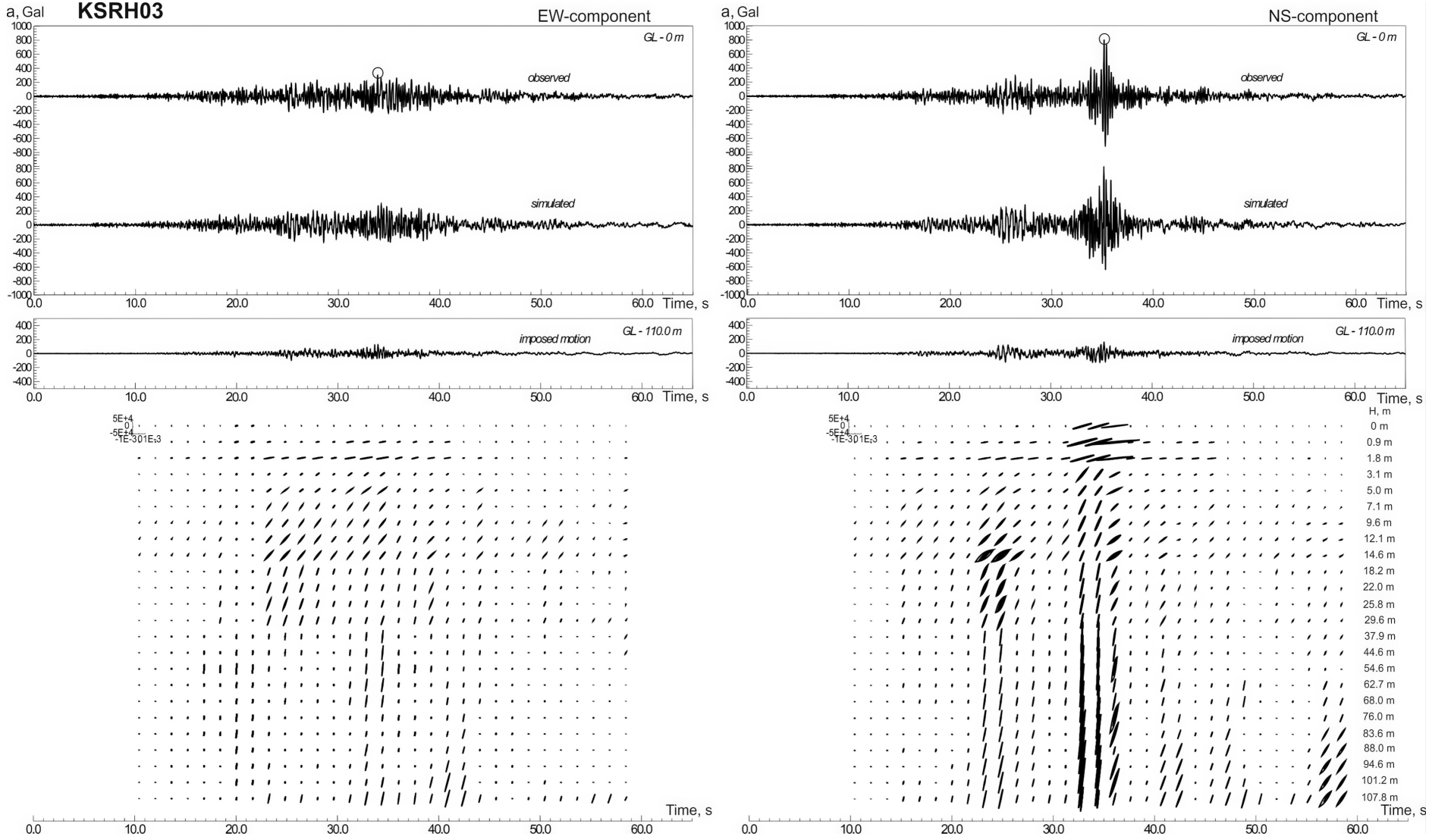

Figure 7. Acceleration time histories of the 2003 Tokachi-oki earthquake, observed and simulated at soft soil site KSRH03, and estimated stress-strain relations in soil layers changing with time during strong motion. Stresses are given in Pa, strains in strain [from *Pavlenko*, 2022] (107.8 m). Each curve corresponds to 1.5-second time interval.

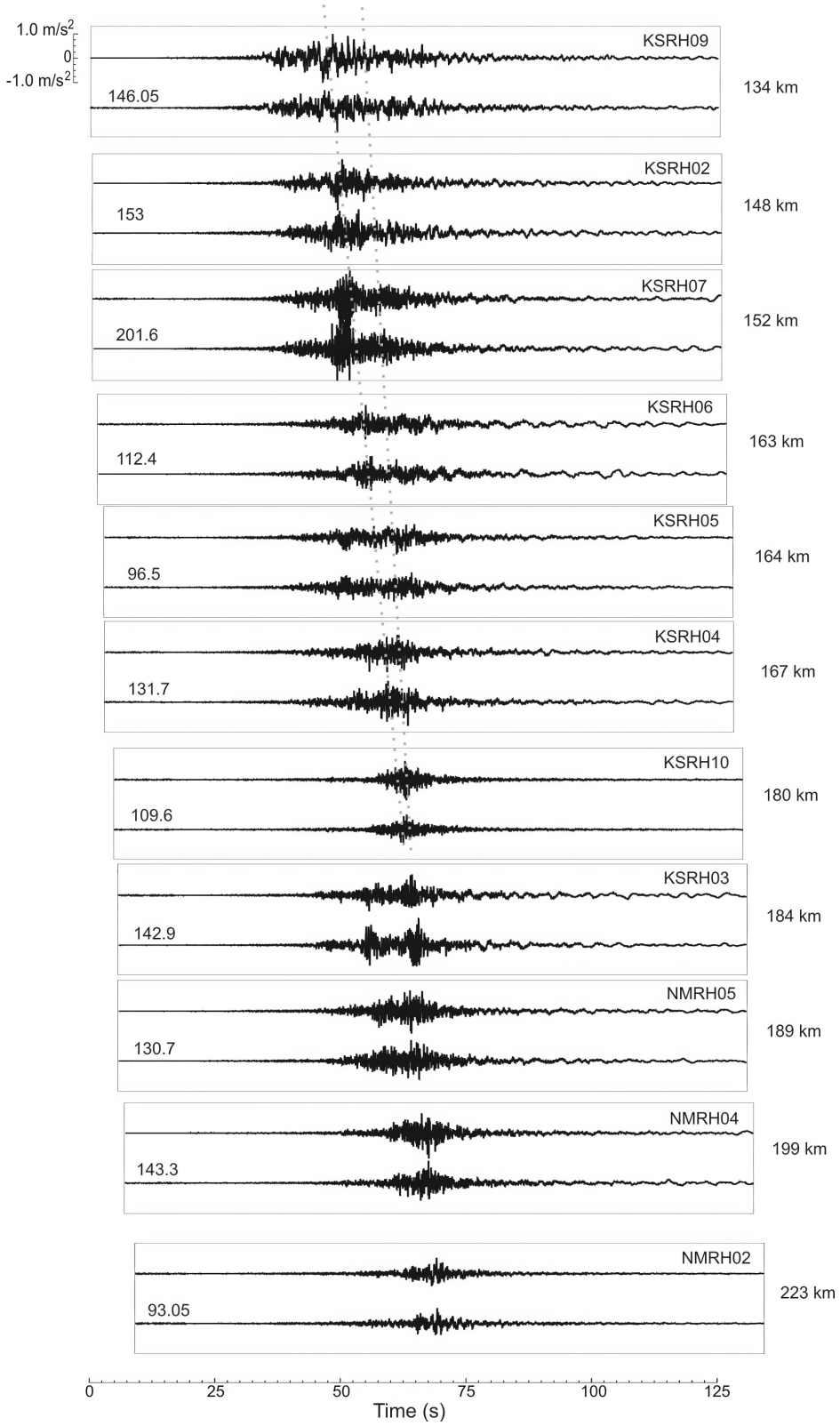

Figure 8. Acceleration time histories (EW and NS components, records of the deep devices) of the 2003 Tokachi-oki earthquake at KiK-net sites located to the north of the epicenter. The traces are arranged according to the distance from the source (vertically) and to the beginning of strong motion (horizontally). For each site, the epicentral distances (on the right) and PGA values in cm/s^2 (on the left) are shown. Dotted lines show the decrease of strong motion duration with distance [from *Pavlenko*, 2022].

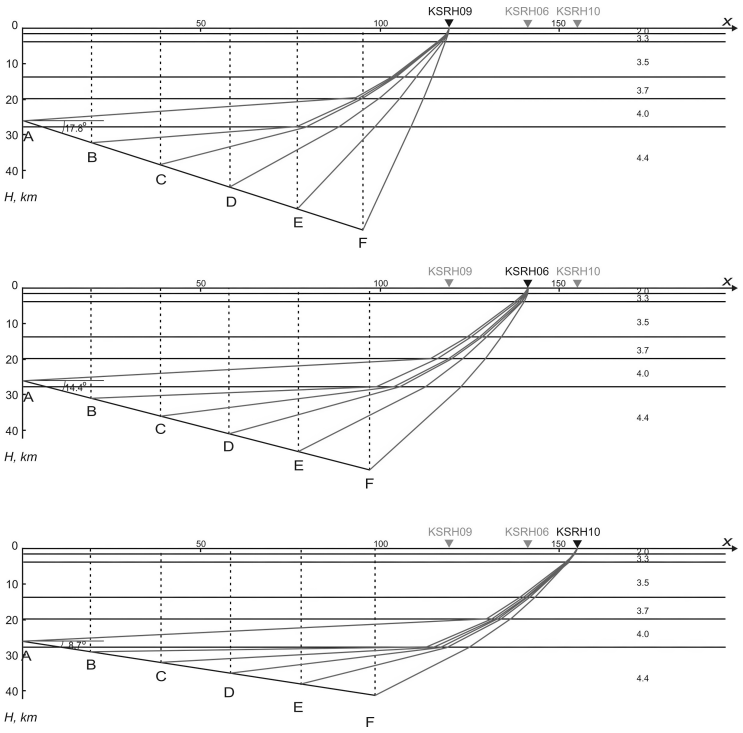

Figure 9. The cross-section of the fault plane of the 2003 Tokachi-oki earthquake, locations of KiK-net sites and seismic wave paths. The numbers indicate *S*-wave velocities in the layers in mm/s; velocity structure model is taken from [*Koketsu et al.*, 2014]. *S*-wave propagation (from top to bottom) – to KSRH09 site, to KSRH06 site, to KSRH10 site [from *Pavlenko*, 2022].

The Noto Earthquake of January 1, 2024

During recent strong earthquake in Japan that occurred on January 1, 2024, with the epicenter at Noto Peninsula and magnitude $M_w \sim 7.6$ (Figure 10), directivity effects were also observed, as seen from the waveforms of acceleration time histories and abnormally high PGA ~2828 Gal recorded at remote station ISK006 (Figure 11).

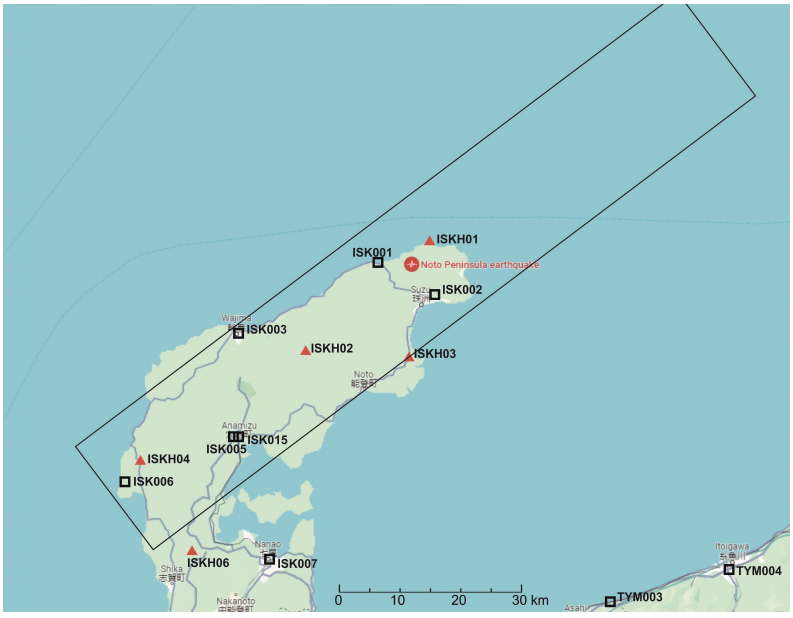

Figure 10. Map showing the location of the earthquake epicenter (red circle), KiK-net (red triangles) and K-NET (black squares) stations in the near-fault zones, and the boundaries of the fault plane, according to USGS (rectangle) [from *Pavlenko*, 2024].

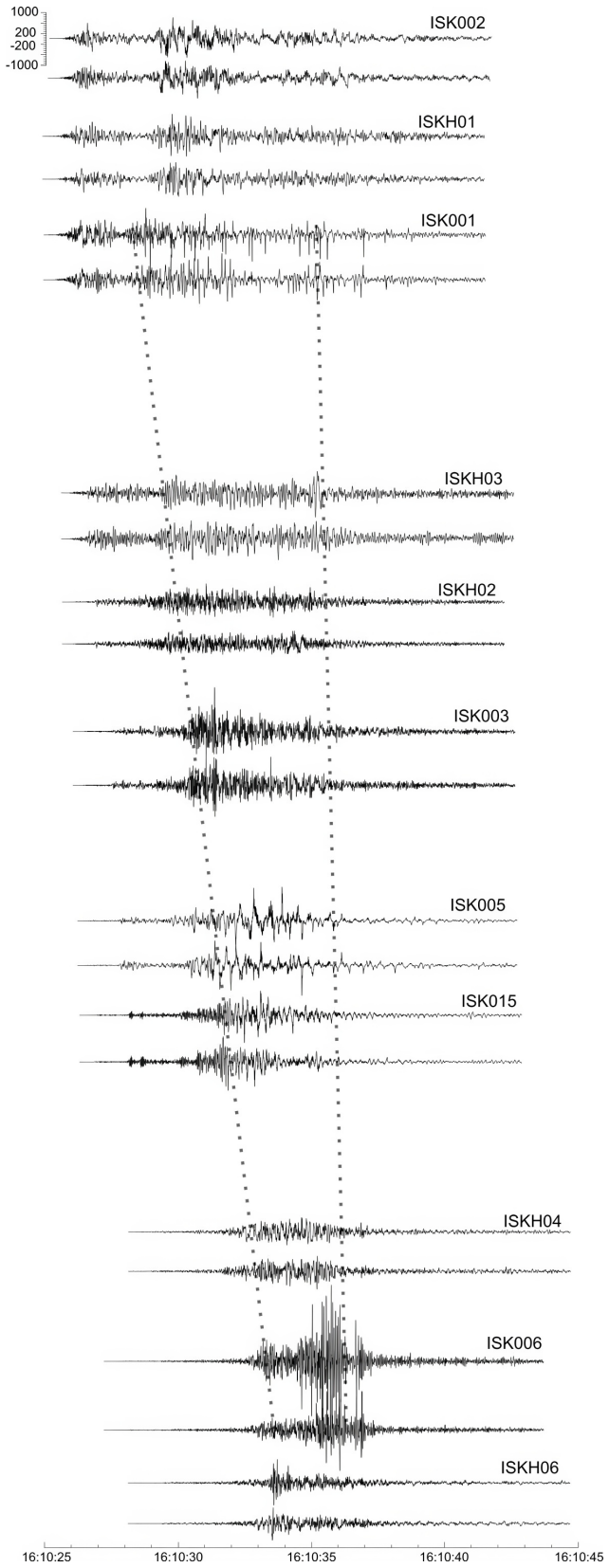

Figure 11. Acceleration time histories of the 2024 Noto earthquake recorded by K-NET and KiK-net stations on the surface in the near-fault zones and arranged in ascending order of epicentral distance, from 2 to 60 km. PGA near the epicenter (at ISK001 and ISKH01 sites, at epicentral distances of 2 km and 8 km) reached ~1470 Gal, and at ISK006 site, at epicentral distance of ~60 km, PGA reached ~2828 Gal [from *Pavlenko*, 2024].

Fortunately, during these subduction earthquakes, the strong motions retained high-frequency characteristics, even on soft soils. This resulted in relatively low amplitudes within the 0.5 to 1 Hz frequency range, which is typically hazardous for buildings. Additionally, due to the fault plane geometry, shock wave fronts were formed at considerable distances from the epicenter. Consequently, the amount of structural damage due to shaking remained relatively low.

Effects of Source Radiation Directivity During Large Crustal Earthquakes (Examples of Earthquakes in Turkey in 2023)

The most comprehensive data on the effects of source radiation directivity during large crustal earthquakes were obtained during the earthquakes in Turkey in February 2023. The sequence began on February 6, 2023, with the main shock M_w 7.8, followed by thousands of aftershocks.

The strongest seismic events occurred within the first twelve hours, with two M_w 7.0+ events having epicenters approximately 100 km apart. These earthquakes induced ground motions that were highly destructive to structures, so-called "pulse waveforms", and the epicentral distances were not a good indicator of the wave attenuation in this case.

Analysis of the obtained records of dense networks of seismic observations AFAD (Ministry of Interior Disaster and Emergency Management Presidency, Figure 12) revealed that at large epicentral distances, strong motion often exhibited no significant attenuation, obviously due to the effects of source directivity [*Baltzopoulos et al.*, 2023a,b].

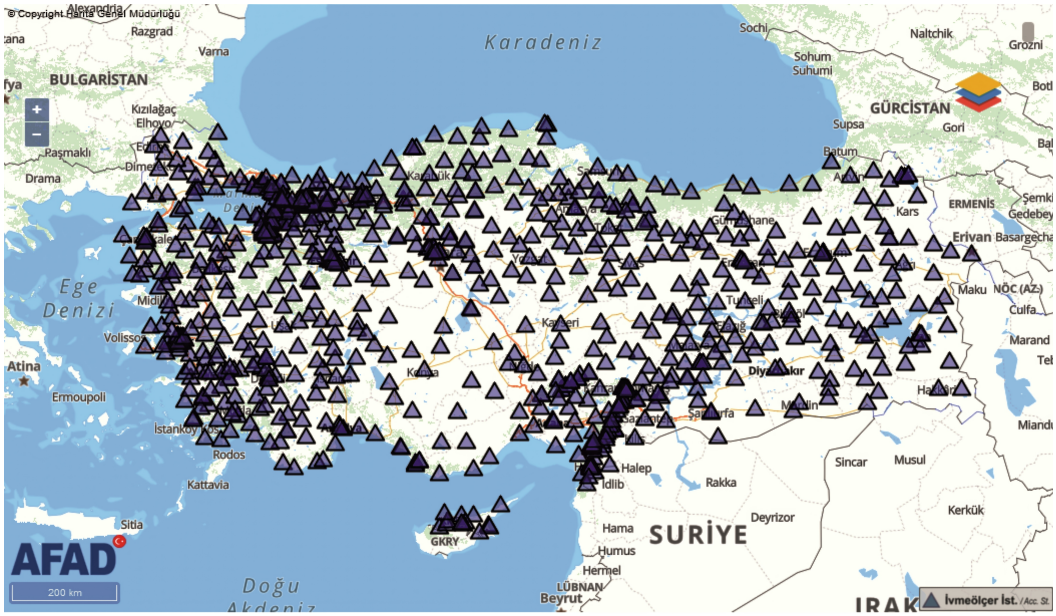

Figure 12. Dense networks of seismic observations in Turkey (taken from AFAD web-site).

The M_w 7.8 earthquake was larger and more destructive than had been expected for the current tectonic setting in that area. Analyzing strong motion records obtained in the near-fault zones, Rosakis and co-authors traced an early transition to super-shear rupture propagation (~1.55Vs) on the splay Narli fault, where the rupture originated. The early transition to the super-shear stage (at an epicentral distance of ~19.5 km) might have facilitated the continued propagation and initiation of slip on the nearby East Anatolian fault (Figures 13 and 14) [*Rosakis et al.*, 2023].

A two-dimensional dynamic rupture model of the earthquake fault was constructed based on the near-field seismic records, field tectonic studies and geometric features of the fault trace [*Abdelmeguid et al.*, 2023]; the model reflects the key features of the complicated M_w 7.8 event and provides high estimates of peak ground velocities (PGV) in near-fault zones (Figure 15).

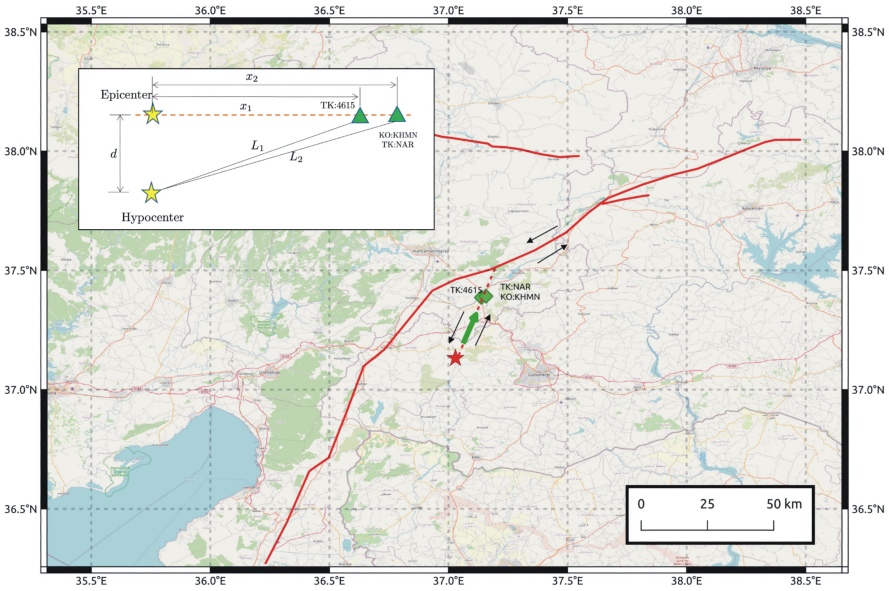

Figure 13. Map of the East Anatolian Fault (EAF) zone, the estimated location of the hypocenter (red star) of the M_w 7.8 Kahramanmaraş earthquake. The dashed line represents the inferred splay fault trace based on AFAD records. Green diamonds indicate the locations of the seismic stations. The black arrows indicate the lateral motion of the fault. The insert is a schematic illustration of the stations layout [from *Rosakis et al.*, 2023].

The geometrical complexity of the fault, the triggering of segmented faults, and unattenuated shock fronts due to super-shear crack propagation contribute to a broader distribution of ground shaking. The more extensive surface failure correlates with regions of wider and more intense ground shaking. Of course, the failure may also be influenced by such phenomena as soil and basin amplification, in addition of course to the type and quality of construction. The landslide and soil liquefaction distribution models provided by USGS are also consistent with coseismic landslides formed by the earthquakes and with liquefied areas obtained from remote sensing [*Taftsoglou et al.*, 2023].

Pulse-Like Features

In regions with super-shear crack propagation, strong motion records show a relatively narrow dominant pulse (1–2 seconds), such as in Antakya at the southern end of the fault, with an amplitude of approximately 2 m/s. This feature was not observed in areas with sub-Rayleigh crack propagation. The presence of a relatively narrow velocity pulse imposes higher demands on structures, significantly increasing the probability of collapse. The records also indicate significant soil destruction associated with both liquefaction and coseismic landslides. Similar patterns were observed in several directions, extending northward toward Malatya.

Geotechnical engineers consider pulse-like ground motions as a distinct type of ground motion capable of causing severe structural damage. These pulses arise from directivity effects when a rupture on the fault plane propagates towards an observation point (forward propagation), typically being more prominent in the fault-normal horizontal components. Directivity effects can occur during earthquakes of various source mechanisms, including strike-slip, dip-slip, normal, and reverse faulting [*Somerville*, 2003, 2005; *Somerville et al.*, 1997; *Spudich and Chiou*, 2008].

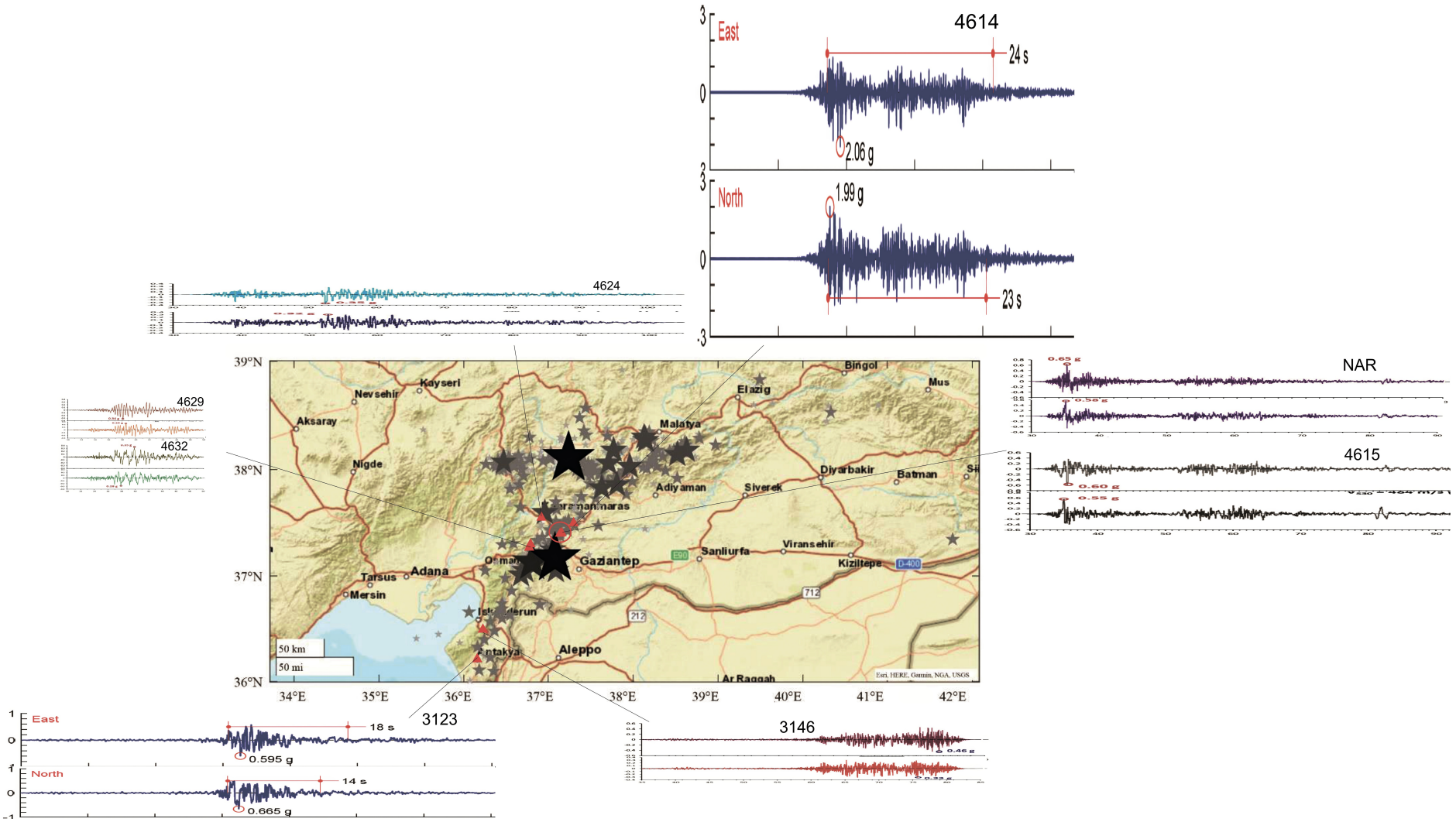

Figure 14. Epicenters of M_w 7.0+ events and the aftershocks (black and gray stars) showing the fault plane of the main shock [from *Baltzopoulos et al.*, 2023b] and accelerograms (horizontal components) from seismic stations closest to the epicenter of M_w 7.8 event [from *Garini and Gazetas*, 2023; *Malhotra*, 2023].

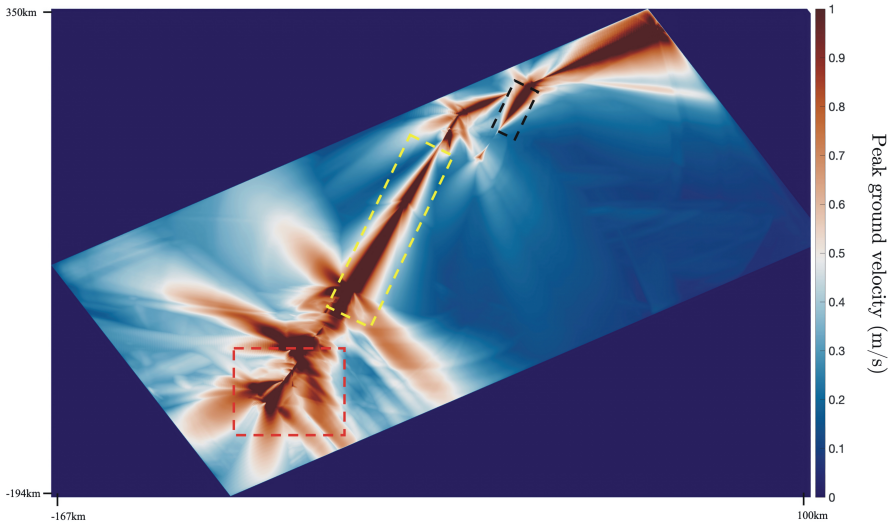

Figure 15. The distribution of PGV obtained from numerical simulation of dynamic rupture [from *Abdelmeguid et al.*, 2023].

Baltzopoulos et al. [2023a,b] analyzed seismic records obtained in the near-fault zones of Turkey earthquakes, focusing on identifying the presence of pulse-like waveforms. The resulting velocity vector at horizontal components rotated by more than 180° with a step of 1° was studied. For each orientation, a combined algorithm of wavelet analysis was applied to identify possible pulse-like waveforms in velocigrams [*Baker*, 2007], and the so-called pulse index (PI), i.e., a numerical parameter indicating the presence of pulse-like waveforms in the record, was estimated. Ground motions were classified as pulse-like if they consistently exhibited a high score of PI > 0.90 across an arc spanning more than 60°, along with a satisfactory match between the pseudo-velocity spectra of the ground motion and a potential pulse wavelet at pulse periods (T_p) [*Baltzopoulos et al.*, 2020]. Consequently, a number of records were identified as pulse-like (Figure 16).

Pulse-like ground motions significantly amplify the response spectra of engineering structures, usually within a narrow frequency band, transferring the structure into the inelastic state at these specific frequencies. Consequently, these motions pose a greater threat to structures compared to non-pulse ground motions, at least on average [*Baez and Miranda*, 2000; *Iervolino et al.*, 2012; *Shahi and Baker*, 2011].

Thus, pulse-like ground motions impose serious demands on structures and have been responsible for significant damage during past strong earthquakes [*Akkar et al.*, 2005; *Alavi and Krawinkler*, 2001; *Anderson and Bertero*, 1987; *Bertero et al.*, 1978; *Hall et al.*, 1995; *Iwan*, 1997; *Luco and Cornell*, 2007; *Makris and Black*, 2004; *Mavroeidis et al.*, 2004; *Menun and Fu*, 2002].

The influence of pulse-like features in velocigrams observed in the near-fault zones on engineering structures was first demonstrated by Mahin and Bertero during the 1971 San Fernando earthquake [*Bertero et al.*, 1977; *Mahin et al.*, 1976]. After the 1979 Imperial Valley earthquake, *Anderson and Bertero* [1987] identified the velocity increment as an important parameter affecting the maximum inelastic response of structures exposed to strong motions in the near-fault zones.

When a rupture transfers from sub-Rayleigh to super-shear crack propagation, there is a sub-Rayleigh signature following the leading super-shear rupture. As a consequence, a building at a near-fault location will first experience the intense shaking due to the shock waves of the super-shear rupture front. These shocks pass very quickly (narrow velocity pulses) and are characterized by the fault-parallel component of the ground velocity being much higher than the fault-normal component. Notice the huge disparity in PGV on the fault-parallel (PGV_{FP}) and fault-normal (PGV_{FN}) components (~ 2 times) at station 3129 in Antakya, where the city was almost destroyed. Seconds later, the building will also experience shaking of a different type, associated with the passage of the trailing Rayleigh

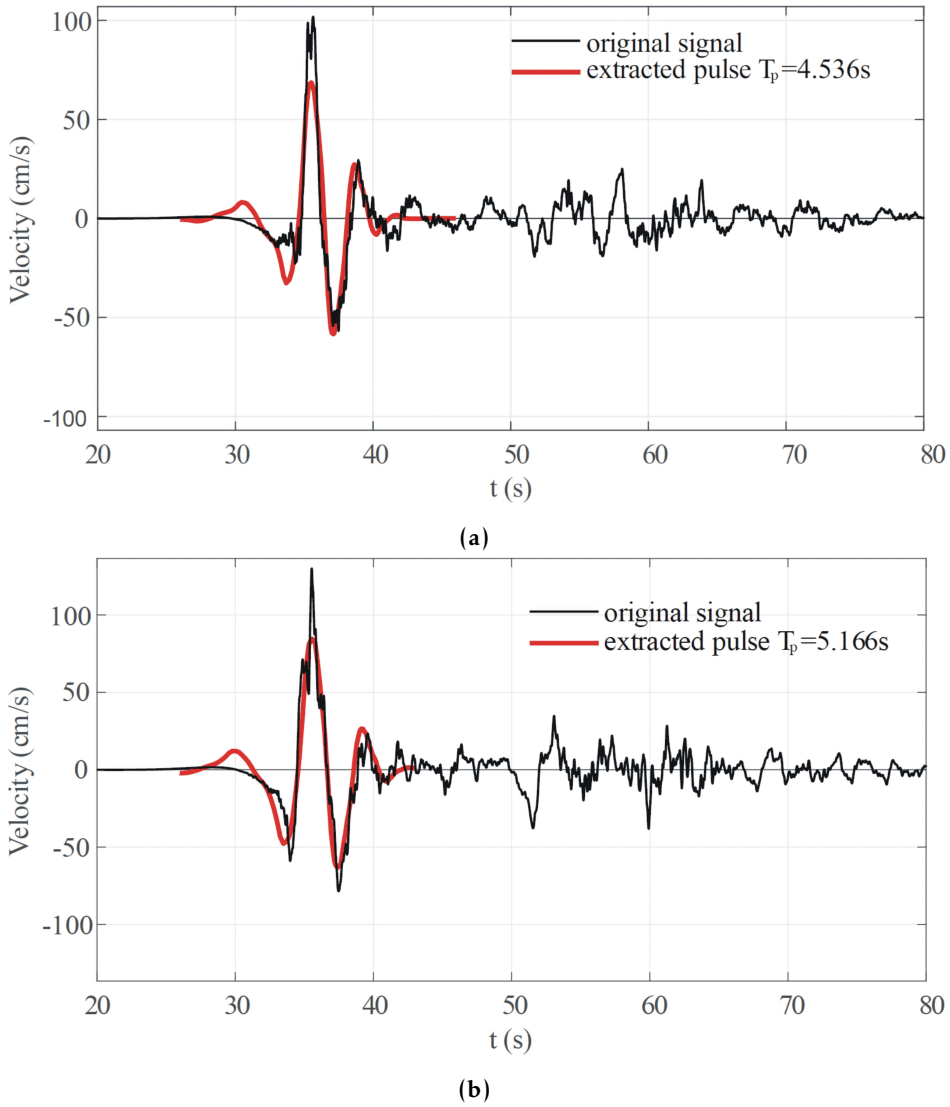

Figure 16. Identified pulse-like velocigrams at stations NAR (a) and 4615 (b) [from *Baltzopoulos et al.*, 2023b].

rupture, with a dominant fault-normal component. This double punch effect can have a devastating impact on the structure. The effects of super-shear ruptures on the ground and structures require further research.

Accounting for Directivity Effects in Seismic Hazard Analysis (SHA) and the Building Codes

Since the late 1990s, seismologists are trying to incorporate the effects of radiation directivity of extended sources of strong earthquakes into SHA procedures.

The study of theoretical dislocation models to understand the kinematics of ground motion in near-fault zones has been ongoing for a considerable time [*Anderson and Bertero*, 1987]. However, following the 1994 Northridge and the 1995 Kobe earthquakes, research in this area significantly accelerated, driven by the need to better comprehend and model the complex ground motion phenomena observed in these events. The analysis of near-fault records and verification by broadband modeling enabled the development of proposals to quantify these effects. These proposals aim to adjust existing empirical attenuation relations to account for the directivity effects on average [*Somerville et al.*, 1995] and specifically for directivity effects of forward rupture propagation [*Abrahamson*, 1998; *Somerville et al.*, 1996].

Directivity effects appearing in amplification of ground motion in areas located in the direction of rupture propagation, are defined by the geometry and size of the fault, the locations of the crack nucleation point and the observation point, the crack propagation velocity, and the frequency contents of the interfering seismic waves. As mentioned above, ground motions enhanced by directivity effects can be extremely destructive [*Kalkan and Kunnath*, 2006; *Mavroeidis and Papageorgiou*, 2003].

One of the first models accounting for the directivity effects in ground motion prediction equations (GMPE) was proposed by *Somerville et al.* [1997]. These authors considered strike-slip and dip-slip faults separately. They assumed that variations of the amplitudes of motion in the near-fault zones are determined by two parameters, namely (1) the angle between the direction of crack propagation and the direction of wave propagation from the source to the observation point (φ for dip-slip faults, θ for strike-slip faults); (2) the part of the width d (for dip-slip faults) or length s (for strike-slip faults) of the rupture surface lying between the hypocenter and the observation point. The corresponding directivity parameters for the two types of slip take the form: $X = \left(\frac{s}{L}\right)\cos\theta$, $Y = \left(\frac{d}{W}\right)\cos\varphi$, where L and W are the length and the width of the fault plane, respectively. Then the corrections to the estimates of the acceleration response spectrum amplitudes are:

$$y = C_1 + C_2 X, \quad y = C_1 + C_2 Y,$$

where C_1 and C_2 are frequency-dependent regression coefficients.

Within the framework of this model, it was assumed that in case of a strike-slip fault the crack propagates in the strike-parallel direction only, while in case of a dip-slip fault – along the dip only. Also, the model did not allow evaluation of directivity effects at points located near the edges of dip-slip faults, where the so-called neutral zones were introduced.

To overcome these limitations, a modification of the model was proposed by *Abrahamson* [2000], which constrained the values of the directivity parameters X and Y to 0.4, and *Rowshandel* [2006] proposed a generalization of the model for the case of inhomogeneous multidirectional ruptures, which allowed expanding the scope of the model.

Spudich and Chiou [2008] proposed an analytical model of directivity effects based on the so-called isochrone directivity predictor, IDP:

$$\mathrm{IDP} = CSR_{ri},$$

$$C = \frac{\min(\tilde{c}', 2.45) - 0.8}{(2.45 - 0.8)} \text{ is the normalized isochrone velocity ratio:}$$

$$\tilde{c}' = \left(\frac{\beta}{v_r} - \frac{(R_{\mathrm{HYP}} - R_{\mathrm{RUP}})}{D}\right)^{-1}, \text{ for } D > 0, \ \tilde{c}' = \frac{v_r}{\beta}, \text{ for } D = 0,$$

where v_r is the velocity of rupture propagation, β is the S-wave velocity in the medium, R_{HYP} and R_{RUP} are the hypocentral distance and the shortest distance from the observation point x_s to the rupture surface, D is the distance from the hypocenter x_h to the point on the rupture surface x_c closest to the point of observation.

$$S = \ln[\min(75, \max(s, h))],$$

where s is the distance from the hypocenter x_h to the point x_c, measured along the fault strike, h is the distance from the upper edge of rupture to the hypocenter, measured along the dip.

$R_{ri} = \max(\sqrt{R_u^2 + R_t^2}, \varepsilon)$ is the scalar amplitude of the radiation pattern, where R_t and R_u are the strike-normal and the strike-parallel components of the radiation pattern, $\varepsilon = 0.2$.

The final model of the directivity effect takes the form:

$$f_D = f_R(R_{\mathrm{RUP}}) f_M(M)[a + b \cdot \mathrm{IDP}],$$

where $f_R(R_{\mathrm{RUP}}) = \max\left[0, \left(1 - \frac{\max(0, R_{\mathrm{RUP}} - 40)}{30}\right)\right]$ takes the value 1 for $0 \le R_{\mathrm{RUP}} \le 40$ and decreases linearly to 0 at $R_{\mathrm{RUP}} \ge 70$, $f_M(M) = \min\left[1, \frac{\max(0, M - 5.6)}{0.4}\right]$ takes the value 0 at $0 \le M \le 5.6$ and increases linearly to 1 at $M \ge 6.0$, a and b are the frequency-dependent regression coefficients.

The described procedures to account for directivity effects represent the correction factors to ground motion estimates obtained by using the GMPEs. Therefore, these procedures are equally applicable to deterministic and probabilistic, as well as the neo-deterministic [*Panza and Bella*, 2020] seismic hazard analysis.

Comparing the isochrone directivity predictor model with the models by *Somerville et al.* [1997] and *Abrahamson* [2000], the authors note that the increase and decrease of ground motion predicted by the model approximately corresponds to the estimates of the Abrahamson's model [*Abrahamson*, 2000] and are almost twice as low as the estimates of the model by *Somerville et al.* [1997] for all spectral periods.

In the models described above, the influence of directivity effects is expressed in a monotonous amplification or attenuation of the amplitudes of the acceleration response spectra in a wide range of periods, therefore, such models are sometimes called "broadband".

On the other hand, some authors [e.g., *Iervolino et al.*, 2012; *Somerville*, 2005; *Tothong et al.*, 2007] note that, according to the available observational data, directivity effects manifest themselves in a rather narrow range of spectral periods, close to the period of the waveform pulse (T_p), and such models are called "narrowband".

Developing the approach proposed by *Tothong et al.* [2007], *Shahi and Baker* [2011] proposed a comprehensive procedure for incorporating the effects of pulse-like waveforms into probabilistic seismic hazard analysis (PSHA). The procedure uses an algorithm for identifying pulse-like waveforms [*Baker*, 2007], which eliminates the ambiguity of data interpretation that occurs during the visual analysis of earthquake records. The important elements of the procedure are: the model of the probability of occurrence of pulse-like ground motions at the observation point depending on its location with respect to the earthquake source, the model of the probability of occurrence of pulse-like ground motions of certain orientation, the model of the dependence of pulse period on the earthquake magnitude, and the model of amplification of the components of the acceleration response spectrum depending on the pulse period.

The listed models were calibrated on a subset of pulse-like waveforms from the NGA [*Chiou et al.*, 2008] database identified using the algorithm by *Baker* [2007]. As a demonstration of the application of this procedure, seismic hazard maps in units of spectral acceleration at 5 s period were calculated for a strike-slip fault by using the proposed procedure and by using the conventional PSHA. Based on these results, a map of seismic hazard increments relative to the conventional PSHA in the near-fault zones was calculated. For comparison, a similar increment map was calculated based on the model by *Abrahamson* [2000]. Both maps provided similar values of seismic hazard increments, while the increments obtained by using the described procedure were concentrated in a much narrower areas around the fault than the increments obtained by using the model by *Abrahamson* [2000]. Significant differences were probably due to the refinement of the model of directivity effects supported by a significantly expanded database accumulated after the publications [*Abrahamson*, 2000; *Somerville et al.*, 1997].

Spagnuolo et al. [2016] applied the model of directivity effects of *Spudich and Chiou* [2008] to construct seismic hazard maps in the area around Istanbul. Seismic hazard in this region is defined by the two nearby segments of the North Anatolian Fault, running along the bottom of the Marmara Sea at a distance of ~20 km from Istanbul. The locations of the hypocenter on the fault segments were modeled by random variables with a normal distribution, a uniform distribution, and a distribution based on modeling of crack propagation processes. The results of the analysis indicated that accounting for the directivity effects leads to a significant (up to 25%) increase of seismic hazard estimates, expressed in spectral accelerations at 2 s period for a return period of 475 years.

Many of the listed results [*Baker*, 2007; *Rowshandel*, 2006; *Shahi and Baker*, 2011; *Spudich and Chiou*, 2008; *Tothong et al.*, 2007] became possible thanks to the extensive database of the NGA project, which once again emphasizes the importance of the accumulation and analysis of earthquake records.

Thus, attention has been paid to accounting for the directivity effects in SHA. Various models have been created to assess the influence of these effects on ground motion, and the procedures for the inclusion of these effects in SHA have been formulated. It was shown that increase in seismic hazard estimates in the near-fault zones due to directivity effects can be significant.

However, several controversial issues remain unresolved, with no consensus yet reached. Different authors suggest different values for the magnitude threshold, above which directivity effects are expected to occur: $M > 6.0$, 6.5, or 7.0. There is no consensus on the size of the regions surrounding the faults, where directivity effects are expected to occur. There is also no consensus on whether broadband or narrowband models correctly describe the influence of directivity effects on ground motion. Obviously, the progress in this area can only be achieved with accumulation of sufficient amounts of observational data.

In countries such as the USA, Australia, and New Zealand, building codes for earthquake-resistant design and construction account for the effects of near-fault zones. Ground motion intensity and duration within a few kilometers of the rupture are significantly influenced by several near-fault effects, which introduce unique features absent at more distant sites. Neglecting these effects may lead to substantial underestimation of ground motion strength at near-fault locations. Near-fault features include:

- directivity and polarization effects related to propagation of seismic waves from a moving rupture [*Somerville et al.*, 1997];
- "fault-fling", i.e., the growth of the permanent displacement associated with the fault offset [*Abrahamson*, 2001];
- hanging wall effects associated with dip-slip faults [*Abrahamson and Somerville*, 1996];
- large vertical accelerations, with near-source vertical spectra often exceeding the horizontal spectra at short periods;
- trapping of energy when the faulting penetrates into lower-velocity surface layers.

These features are responsible for large variations of ground shaking for equivalent ground conditions and distances from the fault. Forward-directivity pulses produce large ground velocities, typically from 1.0 to 1.5 m/s, and displacements that are likely to generate large amplitude inelastic response in affected structures.

After the 1994 Northridge earthquake and the 1995 Kobe earthquake, the coefficients accounting for the fault proximity were introduced in the Uniform Building Code (UBC) of the USA [*ICBO*, 1997]. The coefficients vary from 1.0 to 2.0, depending on the type of the fault and the distance to the nearest known seismic source. However, the coefficients were based on the limited data and did not explicitly account for the difference in the action of ground motion in the near-fault zones on elastic and inelastic response of structures. Other design recommendations have introduced coefficients that explicitly account for requirements for maximum inelastic and maximum elastic lateral displacements [*Applied...*, 1996; 1997]. These coefficients allow to estimate maximum inelastic displacements based on the results of linear elastic analysis.

As mentioned above, pulse-like features in velocigrams, recorded in areas located in the direction of forward propagation, create large velocities and displacements in ground motions, which can lead to inelastic response of large amplitudes in affected structures. *Hall et al.* [1995] summarized information from observations of pulses with peak velocities reaching 170 cm/s and demonstrated that such pulses can be especially dangerous for buildings of ~10 to 25 floors in height. Correction of seismic hazard estimates for the near-fault effects is important only for faults that predominantly contribute to seismic hazard at return periods of interest for design. The Californian Category A fault criteria [*Petersen et al.*, 2000] used in UBC 1997 provide a convenient specification of those faults:

class A faults are those capable of producing earthquakes of magnitude 7.0 or greater, and having slip rates of 5 mm/yr or greater. Near-fault motions are usually strongly polarized, with the medium- to long-period pulses being stronger in the strike-normal direction.

For strike-slip earthquakes, the enhanced strength of the fault-normal component is counter to intuition, which suggests that motion along the strike in the direction of the fault displacement should be greater. However, this is true for the permanent offset component of the displacement, but not for dynamic pulses that control the response spectra. For points close to the fault lying virtually along the fault axis, the radiation patterns for strike-slip faulting show a maximum for the tangential component of motion, corresponding to fault-normal motion, but a minimum for the radial component, corresponding to fault-parallel motion. This result, which may seem unexpected, was predicted using dislocation model and first discovered and explained when interpreting accelerograms of the 1966 Parkfield earthquake in California [*Aki*, 1968; *Haskell*, 1969]. For dip-slip earthquakes, the polarization of the directivity pulse and the fault displacement are aligned.

The combination of the directivity and polarization effects results in the forward-directivity strike-normal ground motion at spectral periods above 0.5 s being approximately twice as high as the average acceleration predicted by attenuation relationships that treat directivity as a random effect. The strike-parallel ground motion approximately equals the average given by standard attenuation relationships that ignore these effects [*AS 1170.4 SUPP 1-1993*, 1993; *NZS 1170.5 Supp 1:2004*, 2004].

Large enhanced directivity will apply only for some epicenters, so it would be very conservative to apply maximum directivity effects to all earthquakes, and in building codes, this is taken into account by assuming that about one-third of earthquakes have large directivity and about two-thirds have near-neutral directivity effects.

For long-period structures at locations where directivity effects could be significant, it is recommended that time history analysis is carried out. It should use some acceleration time histories that include directivity effects. Care should be taken with respect to the orientation of the record, as strike-normal and strike-parallel components should not be interchanged. Also, it is important to include records with neutral and/or backward directivity, as their greater durations than for forward-directivity motions may be important for nonlinear response quantities that are sensitive to duration [*AS 1170.4 SUPP 1-1993*, 1993; *NZS 1170.5 Supp 1:2004*, 2004].

Conclusions

In recent decades, the development of dense networks of seismic observations around the world has significantly expanded the database documenting the manifestations of directivity effects in the near field of extended sources during large subduction and crustal earthquakes.

The examples described above demonstrate that during strong earthquakes with extended sources, directivity effects can be as significant in determining surface motion parameters as source effects, paths effects, and local site effects. However, in large subduction and crustal earthquakes, directivity effects manifest themselves differently. In crustal earthquakes, these effects tend to be more destructive, as they typically occur closer to the fault plane and generate higher-intensity shaking.

The building codes of some countries, including the USA, Australia, and New Zealand, account for directivity effects, recognizing the heightened risk they pose to buildings and engineering structures in the near-fault zones of large earthquakes. The destructive impact of directivity effects was clearly demonstrated by the February 2023 earthquakes in Turkey. Building codes that address these effects operate under the assumption that approximately one-third of earthquakes exhibit pronounced directivity effects, while the remaining two-thirds present near-neutral directivity. The criteria of earthquakes likely to exhibit directivity effects are determined: there should be faults capable of producing earthquakes of magnitudes of 7.0 or greater, and having slip rates of 5 mm/yr or greater. For structures with long oscillation periods located in areas where directivity effects can be significant, it is recommended to perform a time history analysis using accelerograms that incorporate directivity effects.

In Russia, seismic zonation maps OSR-2015 indicate that large subduction earthquakes – capable of generating directivity effects with abnormally high PGA values exceeding 1g and pulse-like ground motions – are possible in the Kuril-Kamchatka seismic zone. Similar directivity-prone crustal earthquakes may occur in regions such as Sakhalin, Magadan, Altai-Sayan, the Baikal Rift Zone, and the Caucasus.

Such effects may have been present during the catastrophic 1995 Neftegorsk M_w 7.6 earthquake in Sakhalin, which completely destroyed the city of Neftegorsk within a few seconds. Although there are no records of the earthquake in the near-fault zones, the extreme intensity of the earthquake is evident in the accounts of those who survived: "The impact was so strong that I flew over the table with my chair, flew three and a half meters..." (from the film of online-edition Spectr).

Therefore, when assessing seismic hazard in Russian regions prone to strong earthquakes of M_w 7.0 and higher, it is essential to account for potential increases in seismic intensity due to directivity effects from large, extended fault sources. Studies, such as those conducted in the Istanbul area, suggest that these directivity effects can lead to an increase in seismic intensity by up to approximately 25%.

Acknowledgments. We are grateful to three anonymous reviewers for their valuable comments and suggestions. This work was supported by the RSF (Russian Science Foundation), grant 23-27-00316.

References

Abdelmeguid M., Zhao C., Yalcinkaya E., et al. Dynamics of episodic supershear in the 2023 M7.8 Kahramanmaraş/Pazarcik earthquake, revealed by near-field records and computational modeling // Communications Earth and Environment. — 2023. — Vol. 4, no. 1. — https://doi.org/10.1038/s43247-023-01131-7.

Abrahamson N. A. Seismological aspects of near-fault ground motions // Proceedings of the 5th Caltrans Seismic Research Workshop. — California Department of Transportation, 1998.

Abrahamson N. A. Effects of rupture directivity on probabilistic seismic hazard analysis // Proceedings of the EERI 6th Seismic Zonation Workshop. — Palm Springs, California : EERI, 2000. — P. 6.

Abrahamson N. A. Incorporating effects of near fault tectonic deformation into design ground motions. — a presentation sponsored by EERI Visiting Professional Program, University at Buffalo, 2001.

Abrahamson N. A. and Somerville P. G. Effects of the hanging wall and footwall on ground motions recorded during the Northridge earthquake // Bulletin of the Seismological Society of America. — 1996. — Vol. 86, 1B. — S93–S99. — https://doi.org/10.1785/bssa08601b0s93.

Aki K. Seismic displacements near a fault // Journal of Geophysical Research. — 1968. — Vol. 73, no. 16. — P. 5359–5376. — https://doi.org/10.1029/jb073i016p05359.

Akkar S., Yazgan U. and Gulkan P. Drift estimates in frame buildings subjected to near-fault ground motions // Journal of Structural Engineering. — 2005. — Vol. 131, no. 7. — P. 1014–1024. — https://doi.org/10.1061/(asce)0733-9445(2005)131:7(1014).

Alavi B. and Krawinkler H. Effects of near-fault ground motions on frame structures. — The John A. Blume Earthquake Engineering Center, Department of Civil, Environmental Engineering, Stanford University, 2001. — 301 p.

Anderson J. C. and Bertero V. Uncertainties in establishing design earthquakes // Journal of Structural Engineering. — 1987. — Vol. 113, no. 8. — P. 1709–1724. — https://doi.org/10.1061/(asce)0733-9445(1987)113:8(1709).

Applied Technology Council. ATC-33 Project. NEHRP guidelines for the seismic rehabilitation of buildings (FEMA publication 273). — Washington, D.C. : Federal Emergency Management Agency, 1997.

Applied Technology Council. ATC-40 Seismic Evaluation and Retrofit of Concrete Buildings. Volume 1 and 2. — Seismic Safety Commission, 1996.

Archuleta R. J. and Hartzell S. H. Effects of fault finiteness on near-source ground motion // Bulletin of the Seismological Society of America. — 1981. — Vol. 71, no. 4. — P. 939–957. — https://doi.org/10.1785/BSSA0710040939.

AS 1170.4 SUPP 1-1993. Minimum design loads on structures (known as the SAA Loading Code), Part 4: Earthquake loads - Commentary (Supplement to AS 1170.4-1993). — Standards Australia, 1993.

Baez J. I. and Miranda E. Amplification Factors to Estimate Inelastic Displacement Demands for the Design of Structures in the Near Field // Proceedings of the 12th World Conference on Earthquake Engineering. — 2000.

Baker J. W. Quantitative Classification of Near-Fault Ground Motions Using Wavelet Analysis // Bulletin of the Seismological Society of America. — 2007. — Vol. 97, no. 5. — P. 1486–1501. — https://doi.org/10.1785/0120060255.

Baltzopoulos G., Baraschino R., Chioccarelli E., et al. Near-source ground motion in the M7.8 Gaziantep (Turkey) earthquake // Earthquake Engineering & Structural Dynamics. — 2023a. — Vol. 52, no. 12. — P. 3903–3912. — https://doi.org/10.1002/eqe.3939.

Baltzopoulos G., Baraschino R., Chioccarelli E., et al. Preliminary engineering report on ground motion data of the Feb. 2023 Turkey seismic sequence // Earthquake reports. — 2023b. — P. 1–56.

Baltzopoulos G., Luzi L. and Iervolino I. Analysis of Near-Source Ground Motion from the 2019 Ridgecrest Earthquake Sequence // Bulletin of the Seismological Society of America. — 2020. — Vol. 110, no. 4. — P. 1495–1505. — https://doi.org/10.1785/0120200038.

Bertero V., Mahin S. and Herrera R. Problems in prescribing reliable design earthquakes // Proceedings of the 6th World Conference on Earthquake Engineering. — 1977. — P. 1741–1746.

Bertero V., Mahin S. and Herrera R. Aseismic design implications of near-fault san fernando earthquake records // Earthquake Engineering and Structural Dynamics. — 1978. — Vol. 6, no. 1. — P. 31–42. — https://doi.org/10.1002/eqe.4290060105.

Bouchon M., Bouin M.-P., Karabulut H., et al. How fast is rupture during an earthquake? New insights from the 1999 Turkey Earthquakes // Geophysical Research Letters. — 2001. — Vol. 28, no. 14. — P. 2723–2726. — https://doi.org/10.1029/2001gl013112.

Chiou B., Darragh R., Gregor N., et al. NGA Project Strong-Motion Database // Earthquake Spectra. — 2008. — Vol. 24, no. 1. — P. 23–44. — https://doi.org/10.1193/1.2894831.

Dunham E. and Bhat H. Attenuation of radiated ground motion and stresses from three-dimensional supershear ruptures // Journal of Geophysical Research: Solid Earth. — 2008. — Vol. 113, B8. — https://doi.org/10.1029/2007jb005182.

Furumura T., Takemura S., Noguchi S., et al. Strong ground motions from the 2011 off-the Pacific-Coast-of-Tohoku, Japan (M_w = 9.0) earthquake obtained from a dense nationwide seismic network // Landslides. — 2011. — Vol. 8, no. 3. — P. 333–338. — https://doi.org/10.1007/s10346-011-0279-3.

Garini E. and Gazetas G. The 2 earthquakes of February 6th 2023 in Turkey & Syria. Second Preliminary Report (8-2-23) Emergence of Fault Rupture. Accelerograms NTUA. Greece. — ISSMGE, 2023.

Hall J., Heaton T., Halling M., et al. Near-source ground motion and its effects on flexible buildings // Earthquake Spectra. — 1995. — Vol. 11, no. 4. — P. 569–605. — https://doi.org/10.1193/1.1585828.

Haskell N. A. Elastic displacements in the near-field of a propagating fault // Bulletin of the Seismological Society of America. — 1969. — Vol. 59, no. 2. — P. 865–908. — https://doi.org/10.1785/bssa0590020865.

ICBO. Uniform Building Code. — USA : International Conference of Building Officials, 1997.

Ide S., Baltay A. and Beroza G. C. Shallow Dynamic Overshoot and Energetic Deep Rupture in the 2011 M w 9.0 Tohoku-Oki Earthquake // Science. — 2011. — Vol. 332, no. 6036. — P. 1426–1429. — https://doi.org/10.1126/science.1207020.

Iervolino I., Chioccarelli E. and Baltzopoulos G. Inelastic displacement ratio of near-source pulse-like ground motions // Earthquake Engineering and Structural Dynamics. — 2012. — Vol. 41, no. 15. — P. 2351–2357. — https://doi.org/10.1002/eqe.2167.

Iwan W. Drift Spectrum: Measure of Demand for Earthquake Ground Motions // Journal of Structural Engineering. — 1997. — Vol. 123, no. 4. — P. 397–404. — https://doi.org/10.1061/(asce)0733-9445(1997)123:4(397).

Kalkan E. and Kunnath S. K. Effects of fling-step and forward directivity on the seismic response of buildings // Earthquake Spectra. — 2006. — Vol. 22, no. 2. — P. 367–390. — https://doi.org/10.1193/1.2192560.

Koketsu K., Hikima K., Miyazaki S., et al. Joint inversion of strong motion and geodetic data for the source process of the 2003 Tokachi-oki, Hokkaido, earthquake // Earth, Planets and Space. — 2014. — Vol. 56, no. 3. — P. 329–334. — https://doi.org/10.1186/bf03353060.

Koketsu K., Yokota Y., Nishimura N., et al. A unified source model for the 2011 Tohoku earthquake // Earth and Planetary Science Letters. — 2011. — Vol. 310, no. 3/4. — P. 480–487. — https://doi.org/10.1016/j.epsl.2011.09.009.

Luco N. and Cornell C. Structure-specific scalar intensity measures for near-source and ordinary earthquake ground motions // Earthquake Spectra. — 2007. — Vol. 23, no. 2. — P. 357–392. — https://doi.org/10.1193/1.2723158.

Mahin S., Bertero V., Chopra A., et al. Response of the Olive View hospital main building during the San Fernando earthquake. Report No.: UCB/EERC-76/22. — Earthquake Engineering Research Center. University of California at Berkeley, 1976.

Makris N. and Black C. J. Dimensional analysis of bilinear oscillators under pulse-type excitations // Journal of Engineering Mechanics. — 2004. — Vol. 130, no. 9. — P. 1019–1031. — https://doi.org/10.1061/(asce)0733-9399(2004)130:9(1019).

Malhotra P. M 7.8 Turkey Earthquake of February 6, 2023. — StrongMotion Knowledge, Clarity Inc., 2023.

Mavroeidis G., Dong G. and Papageorgiou A. Near-fault ground motions, and the response of elastic and inelastic single-degree-of-freedom (SDOF) systems // Earthquake Engineering and Structural Dynamics. — 2004. — Vol. 33, no. 9. — P. 1023–1049. — https://doi.org/10.1002/eqe.391.

Mavroeidis G. P. and Papageorgiou A. S. A mathematical representation of near-fault ground motion // Bulletin of the Seismological Society of America. — 2003. — Vol. 93, no. 3. — P. 1099–1131. — https://doi.org/10.1785/0120020100.

Menun C. and Fu Q. An analytical model for near-fault ground motions and the response of SDOF systems // Proceedings of the 7th U.S. National Conference on Earthquake Engineering. — Oakland, California : Earthquake Engineering Research Institute, 2002. — P. 10.

Miyazawa M. Propagation of an earthquake triggering front from the 2011 Tohoku-Oki earthquake // Geophysical Research Letters. — 2011. — Vol. 38, no. 23. — P. L23307. — https://doi.org/10.1029/2011gl049795.

NIED. National Research Institute for Earth Science and Disaster Resilience. — 2011. — URL: http://www.bosai.go.jp/e/index.html.

NZS 1170.5 Supp 1:2004. Structural Design Actions. Part 5 : Earthquake actions – New Zealand – Commentary. — Standards New Zealand, 2004.

Panza G. G. and Bella J. N. NDSHA: A new paradigm for reliable seismic hazard assessment // Engineering Geology. — 2020. — Vol. 275. — P. 105403. — https://doi.org/10.1016/j.enggeo.2019.105403.

Pavlenko O. V. Atypical soil behavior during the 2011 Tohoku earthquake (M_w = 9) // Journal of Seismology. — 2016. — Vol. 20, no. 3. — P. 803–826. — https://doi.org/10.1007/s10950-016-9561-0.

Pavlenko O. V. Possible Mechanisms for Generation of Anomalously High PGA During the 2011 Tohoku Earthquake // Pure and Applied Geophysics. — 2017. — Vol. 174, no. 8. — P. 2909–2924. — https://doi.org/10.1007/s00024-017-1558-2.

Pavlenko O. V. Influence of source directivity and site effects of 2003 Tokachi-oki earthquake on the generation of high PGA in the near-fault zones // Scientific Reports. — 2022. — Vol. 12, no. 1. — https://doi.org/10.1038/s41598-022-16085-7.

Pavlenko O. V. Effects of Source Directivity and Nonlinear Soil Behavior During the January, 1 2024 Noto Earthquake (M_w = 7.5) // Russian Journal of Earth Sciences. — 2024. — Vol. 24. — ES200. — https://doi.org/10.2205/2024es000909.

Pavlenko O. V. and Irikura K. Estimation of Nonlinear Time-dependent Soil Behavior in Strong Ground Motion Based on Vertical Array Data // Pure and Applied Geophysics. — 2003. — Vol. 160, no. 12. — P. 2365–2379. — https://doi.org/10.1007/s00024-003-2398-9.

Pavlenko O. V. and Irikura K. Nonlinear Behavior of Soils Revealed from the Records of the 2000 Tottori, Japan, Earthquake at Stations of the Digital Strong-Motion Network Kik-Net // Bulletin of the Seismological Society of America. — 2006. — Vol. 96, no. 6. — P. 2131–2145. — https://doi.org/10.1785/0120060069.

Petersen M. D., Toppozada T. R., Cao T., et al. Active fault near-source zones within and bordering the state of California for the 1997 Uniform Building Code // Earthquake Spectra. — 2000. — Vol. 16, no. 1. — P. 69–83. — https://doi.org/10.1193/1.1586083.

Rosakis A., Abdelmeguid M. and Elbanna A. Evidence of Early Supershear Transition in the Feb 6th 2023 M_w7.8 Kahramanmaraş Turkey Earthquake From Near-Field Records [Preprint] // EarthArXiv. — 2023. — https://doi.org/10.31223/x5w95g.

Rowshandel B. Incorporating source rupture characteristics into ground-motion hazard analysis models // Seismological Research Letters. — 2006. — Vol. 77, no. 6. — P. 708–722. — https://doi.org/10.1785/gssrl.77.6.708.

Shahi S. and Baker J. An empirically calibrated framework for including the effects of near-fault directivity in probabilistic seismic hazard analysis // Bulletin of the Seismological Society of America. — 2011. — Vol. 101, no. 2. — P. 742–755. — https://doi.org/10.1785/0120100090.

Somerville P. Magnitude scaling of the near fault rupture directivity pulse // Physics of the Earth and Planetary Interiors. — 2003. — Vol. 137, no. 1–4. — P. 201–212. — https://doi.org/10.1016/s0031-9201(03)00015-3.

Somerville P. Engineering characterization of near fault ground motion // New Zealand Society for Earthquake Engineering Conference. — 2005. — P. 8.

Somerville P., Saikia C., Wald D., et al. Implications of the Northridge earthquake for strong ground motions from thrust faults // Bulletin of the Seismological Society of America. — 1996. — Vol. 86, 1B. — S115–S125. — https://doi.org/10.1785/bssa08601bs115.

Somerville P., Smith N., Graves R., et al. Representation of near-fault rupture directivity effects in design ground motions, and application to Caltrans bridges // Proceedings of the National Seismic Conference on Bridges and Highways. — San Diego, California, 1995.

Somerville P., Smith N., Graves R., et al. Modification of Empirical Strong Ground Motion Attenuation Relations to Include the Amplitude and Duration Effects of Rupture Directivity // Seismological Research Letters. — 1997. — Vol. 68, no. 1. — P. 199–222. — https://doi.org/10.1785/gssrl.68.1.199.

Spagnuolo E., Akinci A., Herrero A., et al. Implementing the effect of the rupture directivity on PSHA for the city of Istanbul, Turkey // Bulletin of the Seismological Society of America. — 2016. — Vol. 106, no. 6. — P. 2599–2613. — https://doi.org/10.1785/0120160020.

Spudich P. and Chiou B. S. Directivity in NGA Earthquake Ground Motions: Analysis Using Isochrone Theory // Earthquake Spectra. — 2008. — Vol. 24, no. 1. — P. 279–298. — https://doi.org/10.1193/1.2928225.

Taftsoglou M., Valkaniotis S., Karantanellis E., et al. Preliminary mapping of liquefaction phenomena triggered by the February 6 2023 M7.7 earthquake, Türkiye / Syria, based on remote sensing data. — 2023. — https://doi.org/10.5281/ZENODO.7668401.

Tajima F., Mori J. and Kennett B. L. N. A review of the 2011 Tohoku-Oki earthquake (M_w 9.0): Large-scale rupture across heterogeneous plate coupling // Tectonophysics. — 2013. — Vol. 586. — P. 15–34. — https://doi.org/10.1016/j.tecto.2012.09.014.

Tothong P., Cornell C. A. and Baker J. Explicit directivity-pulse inclusion in probabilistic seismic hazard analysis // Earthquake Spectra. — 2007. — Vol. 23, no. 4. — P. 867–891. — https://doi.org/10.1193/1.2790487.

Zeng H., Wei S. and Rosakis A. A Travel-Time Path Calibration Strategy for Back-Projection of Large Earthquakes and Its Application and Validation Through the Segmented Super-Shear Rupture Imaging of the 2002 M_w 7.9 Denali Earthquake // Journal of Geophysical Research: Solid Earth. — 2022. — Vol. 127, no. 6. — e2022JB024359. — https://doi.org/10.1029/2022jb024359.